Water-in-PDMS emulsion templating of highly interconnected porous architectures for 3D cell culture

Roberto Riesco, Louisa Boyer, Sarah Blosse, Pauline Lefebvre, Pauline Assemat, Thierry Leichle, Angelo Accardo, Laurent Malaquin

Water-in-PDMS Emulsion Templating of Highly Interconnected Porous Architectures for 3D Cell Culture

Roberto Riesco,[†,‡] Louisa Boyer,[†] Sarah Blosse,[†,‡] Pauline M. Lefebvre,[§,∥] Pauline Assemat,[§] Thierry Leichle,[†] Angelo Accardo,[*,†,⊥] and Laurent Malaquin[*,†]

[†]LAAS-CNRS, Université de Toulouse, CNRS, F-31400 Toulouse, France

[‡]Institut National des Sciences Appliquées—INSA, F-31400 Toulouse, France

[§]Institut de Mécanique des Fluides de Toulouse, Université de Toulouse, CNRS, F-31400 Toulouse, France

[∥]FR FERMAT, Université de Toulouse, CNRS, INPT, UPS, F-31400 Toulouse, France

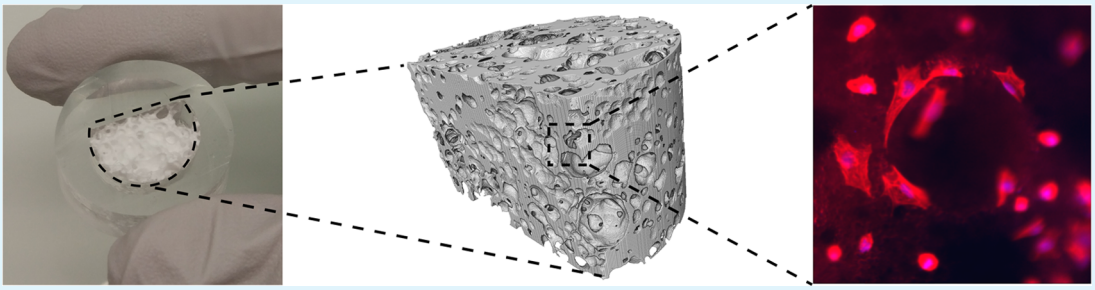

ABSTRACT: The development of advanced techniques of fabrication of three-dimensional (3D) microenvironments for the study of cell growth and proliferation has become one of the major motivations of material scientists and bioengineers in the past decade. Here, we present a novel residueless 3D structuration technique of poly(dimethylsiloxane) (PDMS) by water-in-PDMS emulsion casting and subsequent curing process in temperature-/pressure-controlled environment. Scanning electron microscopy and X-ray microcomputed tomography allowed us to investigate the impact of those parameters on the microarchitecture of the porous structure. We demonstrated that the optimized emulsion casting process gives rise to large-scale and highly interconnected network with pore size ranging from 500 μm to 1.5 mm that turned out to be nicely adapted to 3D cell culture. Experimental cell culture validations were performed using SaOS-2 (osteosarcoma) cell lines. Epifluorescence and deep penetration imaging techniques as two-photon confocal microscopy unveiled information about cell morphology and confirmed a homogeneous cell proliferation and spatial distribution in the 3D porous structure within an available volume larger than 1 cm^3. These results open alternative scenarios for the fabrication and integration of porous scaffolds for the development of 3D cell culture platforms.

KEYWORDS: *PDMS, 3D scaffold, emulsion, porosity, osteosarcoma cells*

1. INTRODUCTION

The development of porous materials has been a major concern for materials science since decades. Their properties play an important role in many applications such as energy storage and conversion, pollutant gas capture, and drug delivery.[1−4] Porous structures are also fundamental in the development of living organisms. Oxygen capture in our bodies is due to the porosity of alveolar tissue in our lungs, which maximizes the exchange surface available for this task.[5] In bones, the trabecular topology works as a niche for the bone marrow and provides a proper environment for cellular regeneration.[6] Further, in the context of the realization of biomimetic scaffolds for cell culture and tissue engineering studies, the accurate tuning of pore distribution and pore size allows the cells to infiltrate easily within the material, promote the perfusion of nourishment, and facilitate the vascularization of the restored tissue.[7] To achieve these topologies, many solutions have been recently proposed in the field of material sciences and, in particular, polymer science.

One of the most extended and widely used materials for bioapplications in the last decades is poly(dimethylsiloxane) (PDMS).[8] Since Wacker Chemie discovered this silicone-based organic elastomer in the 1950 s, it has found a large range of applications starting from lab on chips and microfluidic devices[9] to contact lenses, medical devices,[10,11] alimentary industry, passing through energy storage,[12] flexible electronics,[13−15] and piezoelectric actuators.[16] PDMS is also known for its biocompatibility[17] and molding properties[18] to generate medical devices or even bioimplants.[19] Furthermore, PDMS features a low surface tension and energy, and it is

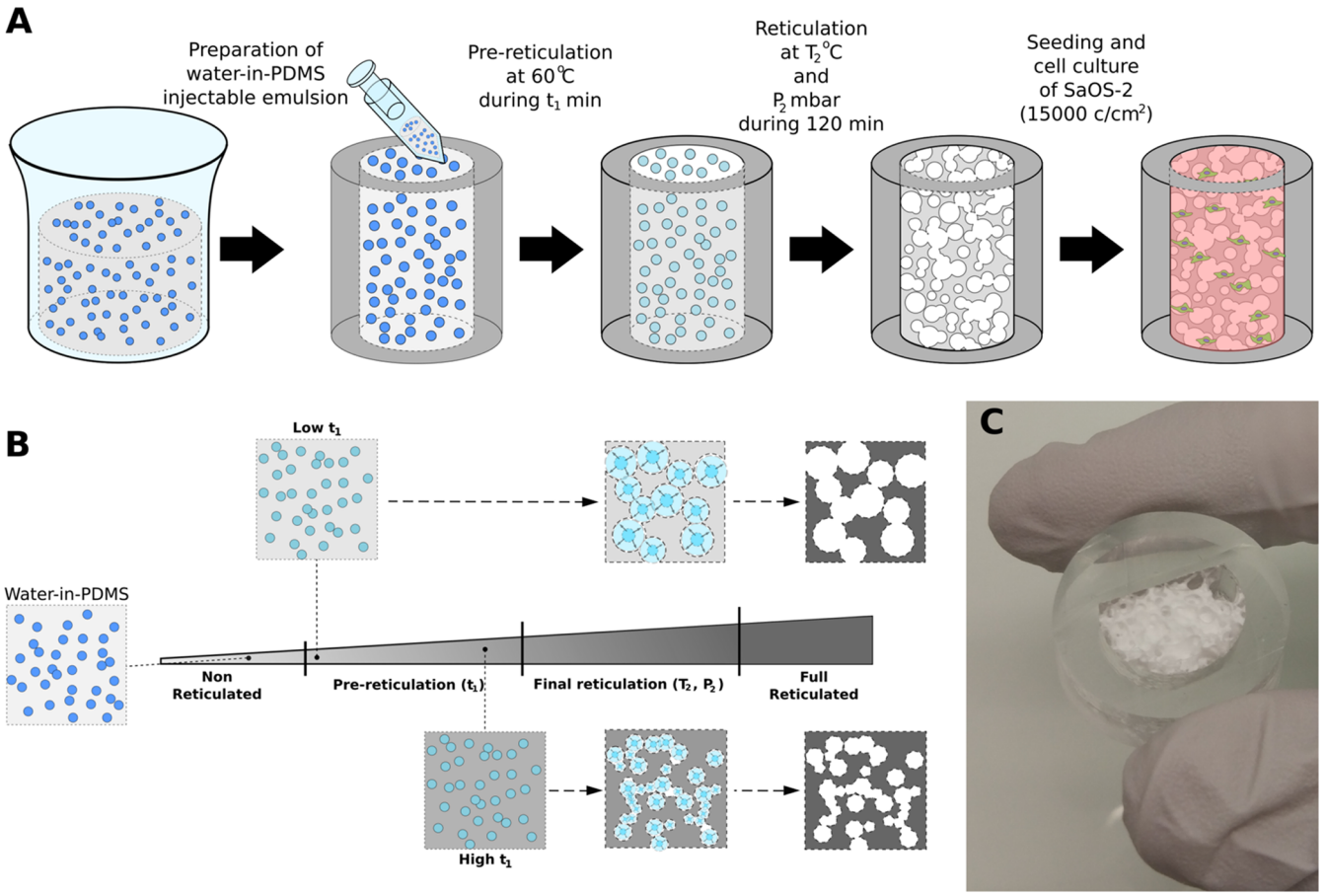

Figure 1. (A) Sketch of the fabrication process of the PDMS porous scaffold. The emulsion is injected into a PDMS shell and placed in an oven at 60 °C for t_1 min. Afterward, the scaffolds are transferred to a vacuum oven at temperature T_2 under pressure P_2. (B) Sketch of the impact of the physical parameters of the fabrication process in the porous morphology. (C) Optical image of the PDMS porous scaffold.

hydrophobic although its surface properties are easily tunable via oxygen plasma treatment to introduce hydroxyl groups, allowing grafting of proteins or other functional groups.[20]

Concerning biological applications, PDMS is well adapted with cell biology applications:[21] it is compatible with almost every technique of protein coating for cell adhesion, and its mechanical properties[18,22] are known to be compatible with cell culture. One of the main advantages over other materials is its permeability to oxygen and water, which allows the cell medium to oxygenate and reach biocompatibility levels.[23] In addition, it is transparent and compatible with optical characterization method and is lowly photoluminescent,[24] allowing the use of fluorescent markers for the visualization of cellular features. For all of these reasons, PDMS is broadly used in biological applications and is undoubtedly one of the main materials used in the fabrication of health sensors, flexible biocontacts, or microfluidic devices for biomedical applications.

Nowadays, one of the main challenges in tissue engineering is to develop models of microenvironments that mimic the key aspects of the architecture and organization of living tissues. Hence, in the past two decades, we witnessed a transition from conventional two-dimensional (2D) Petri dish monolayer cell culture approaches to three-dimensional (3D) architectures featuring topological, mechanical, and biochemical aspects matching the natural growth environment of cells.[25−28] To fulfill this need, material scientists, biomedical engineers, and microfabrication researchers started to investigate and develop protocols aiming at realizing such architectures by exploiting diverse additive manufacturing and other 3D fabrication techniques such as fused deposition modeling and electrospinning,[29] stereolithography,[30,31] direct laser writing,[32−35] or bioprinting.[36] Although most of these approaches allow the fabrication of scaffold features down to the micrometric or even submicrometric scale, they are often limited by the overall printable size of the object, by the cost of the fabrication setup, as well as by the scarcity of biocompatible materials for biological applications.[37] PDMS can be hardly integrated within additive manufacturing processes, and it is not possible to unmold three-dimensional patterns with cell resolution while its biocompatibility for biomedical applications is widely proved. On the other hand, a large community of chemists and material scientists developed fabrication protocols of PDMS sponges based on emulsions/foams,[38] gas foaming,[39] or microcasting of sacrificial materials/structures.[40−43] The important molecular role of the hydrophobic/hydrophilic tails and the tuning of its wettability properties[44] make it a perfect candidate for microfluidic or environmental applications,[45] while some groups have recently tested the possibility of using PDMS macroporous sponges for tissue engineering.[46,47]

In this paper, we report for the first time a simple, rapid, and cost-effective 3D fabrication technique for creating mesoscale porous PDMS scaffolds of centimeter scale, featuring a pore size ranging from millimeter to micrometer scale. The protocol is based on H_2O/PDMS emulsion casting and subsequent

pressure-/temperature-controlled curing. This process is similar to previously reported polymer high internal phase emulsion (polyHIPE) technique;[48,49] however, it relies on a progressive expansion of the internal phase that allowed us to tune the pore size, distribution, and interconnectivity within the architecture. Optical microscopy, scanning electron microscopy (SEM), and X-ray tomography investigations showed an interconnected porous architecture with an available porosity estimated to be higher than 57%. The scaffolds were then tested in the presence of an osteosarcoma cell line, namely, SaOS-2, which holds several osteoblastic features[50] and is commonly employed as an in vitro model for studying the transition of human osteoblasts to osteocytes.[51] The SEM, fluorescence, and two-photon confocal imaging characterizations of both the surface and the inner core of the scaffold revealed an efficient 3D cell colonization of the architecture and the presence of the typical flattened cytoskeletal morphology expected for SaOS-2 cells. The results show how the fast prototyping fabrication protocol that we developed and the tunability of the pore size and pore distribution open a promising scenario for the development of 3D cell culture models and tissue engineering applications involving PDMS.

2. MATERIALS AND METHODS

2.1. Materials. Poly(dimethylsiloxane) (PDMS) was purchased from Dow Corning in a kit containing a silicone base and a curing agent (Sylgard 184). All of the PDMS mixtures presented in this work were prepared following standard proportions (10:1 = base/curing agent w/w) and properly degassed using a dedicated chamber under vacuum. We employed ultrapure (type I) deionized water (DIW) from a Milli-Q Direct purifier system. Molds were fabricated with a 3D stereolithographic system DWS 29J+ in DS3000 and DL260 materials from DWS Systems.

2.2. Fabrication of Standardized PDMS Scaffold Holders. Due to the biological purposes of this work, the dimensions of all of the developed scaffolds were designed to be compatible with standard cell culture consumables configuration. The samples were fabricated to fit inside a 12-well plate (22 mm diameter for each well). To ensure a perfect sealing of the scaffold in the wells and provide a manageable object, a PDMS scaffold holder was fabricated by 3D printing and inserted in the multiwell plate during the casting (see Figure S1 in the Supporting Information) to obtain a cylindrical shell of PDMS with a semicircular empty space where we then injected the water/PDMS emulsion. The height of the scaffold holder was set between 1 and 1.5 cm, while its inner diameter was set to 1.4 cm. PDMS silicone was poured on the plate and cured at 60 °C overnight.

2.3. Emulsion Casting. Highly porous PDMS scaffolds were fabricated by the method of emulsion casting, using water as internal phase, and reticulating the emulsion within specific environmental conditions (Figure 1A,B). Water-in-PDMS emulsion was made by progressively adding small quantities (~10% of PDMS mass) of DIW and mixing until reaching 70% of water-in-silicone. With this process, we generated a water-in-silicone emulsion that was then injected into the cylindrical sample holder. The reticulation process consisted of two separate steps of reticulation by varying temperatures and pressures that allowed us to control the pore size and distribution (Figure 1C): (1) the samples were first placed inside an oven (Memmert) at T_1 = 60 °C for a specific time t_1 ranging from 30 to 60 min in atmospheric pressure condition; (2) the samples were then transferred into a vacuum oven (SalvisLAB Vacucenter) at T_2 ranging between 110 and 130 °C with an absolute pressure value P_2 of 400 or 700 mbar for 2 h. After this time, we did not observe any notable evolution of the size and interconnectivity of the pores. Both edges of the samples were removed by slicing the cylinder with a surgical blade to obtain a clean surface.

2.4. Scanning Electron Microscopy. We used scanning electron microscopy (SEM) to observe the microscopic morphology of the samples with a Hitachi S-4800 system at an accelerating voltage ranging from 2 to 5 kV and 10 μA current. The imaging was performed on core regions of the scaffolds, accessed by cross-cutting the samples with a surgical blade, in flat and 45° tilt-angle SEM sample holder positioning configuration. To improve the resolution and avoid charging effects, the samples were coated with a 15 nm layer of sputtered gold using PECS I from Gatan Systems. False-color imaging treatment was performed by using the open-access software Gimp 2.

2.5. X-ray Tomography. To investigate the pore properties of the sample, X-ray microcomputed tomography (μCT) imaging was performed. μCT is a nondestructive imaging technique that allows quantification of internal features of an object in three dimensions with microscopic resolution. In this study, the specimen was inserted inside a X-ray microtomography machine manufactured by RX Solutions (EasyTom XL 150). A sealed-type microfocus X-ray source with beryllium target was used. The X-ray source energy was adjusted to the resolution of the scan: the source voltage was fixed at 66 kV and source current at 268 μA. Before the acquisition, standard black and gain calibrations were performed. A complete scan was acquired by recording 1440 projections of the sample at different angles, equally spaced on 360°, with a flat panel of 1920 × 1536 pixels. Each projection had average exposure times of 0.11 and 5 s. The 3D volume and corresponding slices were reconstructed with the RX Solutions software, X-Act, using a filtered back-projection algorithm. Reconstructed slices had an isotropic resolution of 18 μm. Postprocessing of images was performed with Avizo 9.7.0, a software dedicated to data visualization, segmentation, and quantification. A nonlocal means filter[52] was first used to remove noise. For the binarization of images, two different methods were used: (1) a user-defined threshold was applied to separate pores and PDMS matrix and extract the binary image on each slice; (2) a watershed algorithm[53] was also applied on filtered images to separate pores and PDMS material. Watershed-based segmentation consists of transforming the gray-level image as a topographic map, where high intensity represents peaks and hills while low intensity represents valleys. The obtained topographic image is then flooded, starting from user-defined seeds, using an automatic gradient magnitude algorithm. Dams are built to avoid merging water from two different catchment basins. The segmentation result is defined by the locations of the dams, i.e., the watershed lines. Porosity in both cases (user-defined threshold and watershed algorithm) was finally calculated as the fraction of pore volume over the total volume of the specimen. The connectivity of pores was evaluated with the Axis Connectivity function available on Avizo.

2.6. Water Retention. To complement the results obtained by X-ray microcomputed tomography, an empirical test was completed to provide experimental data about the absorbance of water within the 3D architecture. The porous PDMS scaffolds were dried in a vacuum oven at 60 °C overnight and then weighted to obtain W_{dry}. The PDMS was plasma-activated using oxygen plasma treatment (Diener Electronic, 5 sccm oxygen flow, 0.5 mbar, 5 min, 50 W) to enhance wettability and immediately soaked in PBS over 48 h. The water retained in the scaffold was measured using an electronic balance that provided us with W_{wet}. The percent of water remaining in the porous PDMS scaffold was calculated as[54]

$$\text{water retention (\%)} = \frac{(W_{wet} - W_{dry})}{W_{dry}} \times 100$$

2.7. Cell Culture, Fixation, and Staining. Prior to cell culture, the porous PDMS scaffolds were first sterilized for 1 h under UV exposure at 254 nm. The PDMS surface was then activated with an oxygen plasma treatment (Diener Electronic, 5 sccm oxygen flow, 0.5 mbar, 5 min, 50 W) and coated with 10 μg/mL of human fibronectin (Corning) for 1 h at room temperature. The osteosarcoma cell line (SaOS-2) was obtained from the American Type Culture Collection (ATCC) and grown using minimum essential medium α (α-MEM)

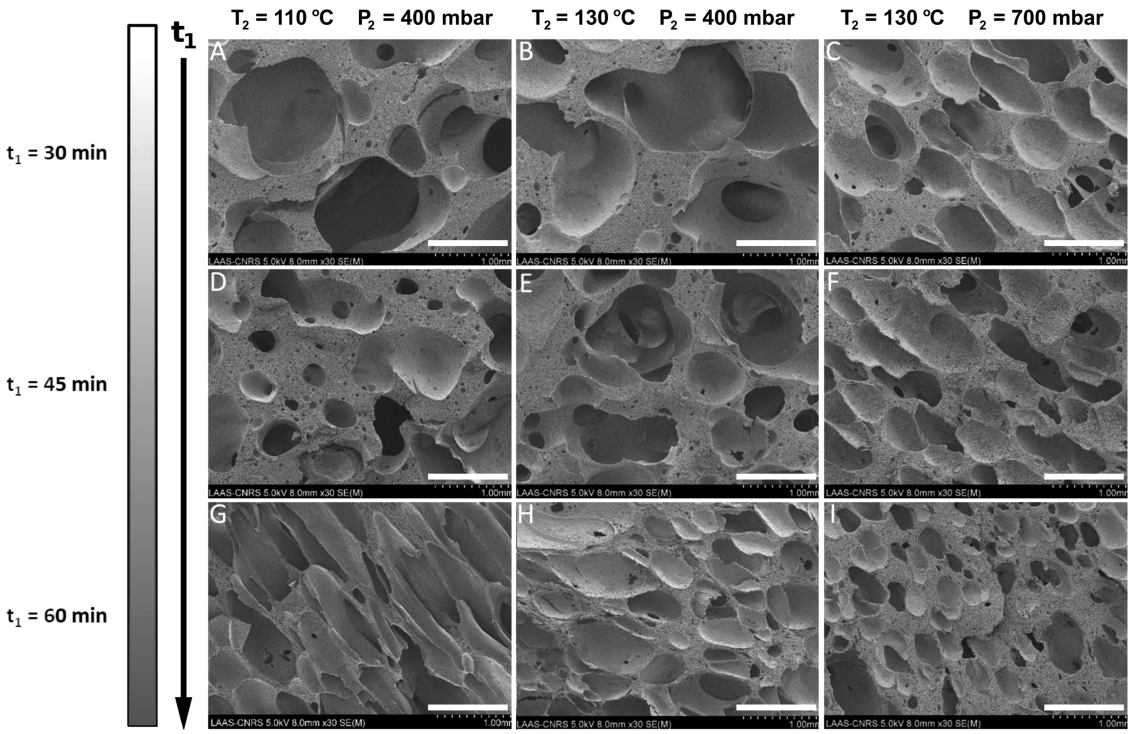

Figure 2. SEM characterization of the cross-sectional regions in the PDMS porous scaffold for different curing parameters. Along the vertical axis, we vary the time t_1 for the prereticulation stage at 60 °C. Along the horizontal axis, we vary the temperature T_2 and the pressure P_2 of the second reticulation process. The scale bar is 1 mm.

containing nucleosides, GlutaMAX, (Gibco, Fisher Scientific) supplemented with 10% fetal bovine serum (HyClone, Fisher Scientific) and 1% penicillin/streptomycin mix (Gibco, Fisher Scientific). A cell suspension (15 000 cells/cm^2) was deposited in a droplet of supplemented α-MEM on top of the PDMS porous scaffold and incubated in an atmosphere containing 5% CO_2 at 37 °C for 1 h to enable the cells to adhere to the scaffold. Multiwell plates were then filled with additional supplemented α-MEM and incubated for 72 h. To prepare the sample for SEM characterization, cells were rinsed with PBS 1× (phosphate-buffered saline) solution and incubated in 4% glutaraldehyde (Sigma) solution for 4 h at room temperature. The cells were then dehydrated by incubation in 50, 70, 90, and 100% ethanol solutions for 4 min at each step and dried for few hours at room temperature to remove alcohol residues. Immunofluorescence staining was performed as follows: cells were rinsed with PBS 1×, fixed with 10% formalin solution (Sigma) for 30 min, permeabilized in 0.2% Triton X-100 for 3 min, and blocked in 3% BSA for 30 min. The samples were then incubated in phalloidine−rhodamine (Invitrogen, Fisher Scientific) at 1/200 dilution in PBS 1× for 30 min at 37 °C to stain the F-actin (protein of the cell cytoskeleton) and then in a DAPI (Thermo Scientific, Fisher Scientific) solution at 1/100 dilution in PBS 1× for 5 min at room temperature to stain the DNA in the nuclei. After staining, the cells were stored in PBS 1× solution at 4 °C. In an additional protocol for two-photon confocal imaging, the cells were rinsed with PBS 1×, stained with a mix of Hoechst (Invitrogen, Fisher Scientific) at 5 μg/mL plus CMFDA (Invitrogen, Fisher Scientific) at 1/1000 dilution in DMEM without phenol red (Gibco, Fisher Scientific), incubated for 30 min at 37 °C, rinsed again with PBS 1×, and fixed for 30 min in 10% formalin solution (Sigma). The samples were stored in PBS 1× at 4 °C prior to imaging. Cytocompatibility was assessed by Live/Dead assay in the porous PDMS scaffold choosing flat PDMS and glass as control. All samples followed the protocol of plasma treatment and fibronectin coating mentioned above. After 72 h of culture in supplemented α-MEM, the samples were rinsed in PBS and cells were stained with calcein/ethidium (Live/Dead viability kit for mammalian cells, Fisher Scientific) diluted in DMEM without phenol red for 30 min and then rinsed with the same medium for fluorescence characterization.

2.8. Immunofluorescence Characterization. Two different immunofluorescence imaging techniques were employed to investigate the cell distribution and proliferation taking place on the 3D PDMS scaffolds. 2D observations of the scaffolds' surface were performed using an Olympus C211 fluorescence microscope equipped with a X-Cite 120 Hg lamp, a BP (300−400 nm) filter for DAPI, a BP (575−595 nm) filter for calcein, a BP (518−573 nm) filter for phalloidin rhodamine/ethidium, and 5×, 10×, 20× and 50× objectives. 3D imaging of the scaffolds were performed using a two-photon confocal imaging system (AxioImager upright microscope LSM 7MP, Carl Zeiss). A pulsed femtosecond Ti:sapphire laser (Chameleon Ultra II; Coherent) tunable in the range of 690−1064 nm was used as excitation light source. Z-stack acquisitions were performed with a 10× W-Plan Apochromat air objective with 0.45 N.A. and a laser excitation wavelength tuned at 800 nm. An automatic z-compensation of the laser power was applied to provide a homogeneous imaging of the imaged volume of the 3D scaffold. Emitted light was detected through a descanned pathway leading to two nondescanned detectors and emission was recorded simultaneously with two emission filters: a band pass (BP) filter, set at 500−550 nm (green channel, CMFDA), and a short-pass (SP) filter set at 485 nm (blue channel, DAPI). Image processing and 3D reconstruction were performed by ImageJ and Imaris (Version 8.2, Bitplane) softwares.

3. RESULTS AND DISCUSSION

3.1. Morphological Characterization of the PDMS Scaffolds. In Figure 2, we report how the tuning of the fundamental curing parameters (t_1, along the vertical axis, and T_2−P_2, along the horizontal axis) affects the morphology of the PDMS porous scaffolds. The increment of the prereticulation process time affects the pore size and distribution as highlighted by comparing the rows of each column. The first row of Figure 2A−C, related to t_1 = 30 min, shows a typical

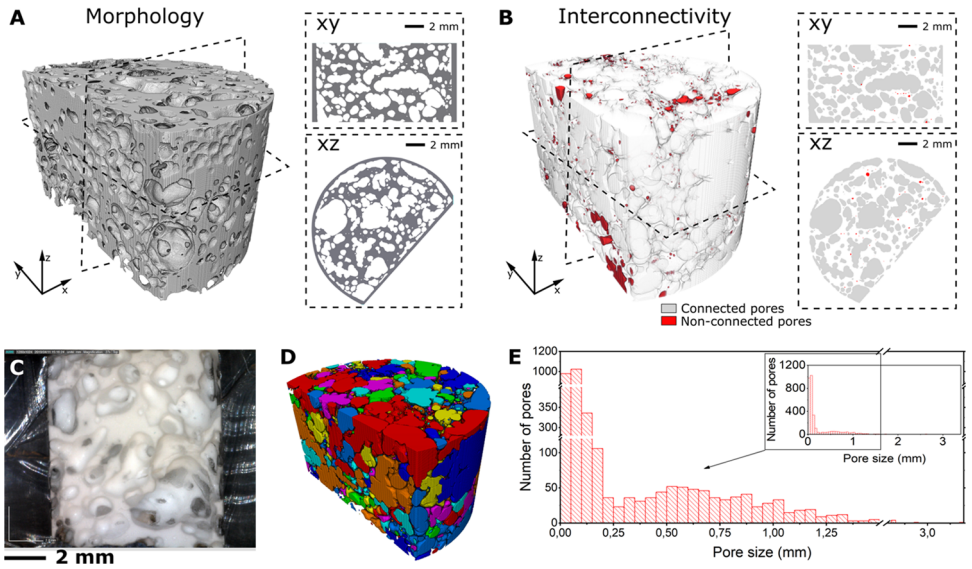

Figure 3. (A) 3D view of the PDMS scaffold after segmentation process. On the right, crosscuts of the reconstruction along the *xy* and *xz* planes. (B) 3D view of the pores: nonconnected pores (red), connected pores (white). On the right, crosscuts of the reconstruction along the *xy* and *xz* planes. (C) Optical micrograph of the inner core of a PDMS porous scaffold. (D) 3D colorimetric view of the pores size distribution with a watershed-based algorithm. (E) Distribution of the number of pores according to the pore size depicted in (D).

pore size of 1−3 mm with few submillimetric pores observable. When increasing t_1 up to 45 min, this pore size distribution slightly decreases (Figure 2D−F) down to 0.5−2 mm, while we observe at the same time an increased number of submillimetric pores. Finally, in the third row of Figure 2G−I, we report a reduction of the pore size coupled to an evident anisotropy of the pore orientation directed toward the open side of the PDMS scaffold holder.

A lower t_1 implies a less reticulated state of the PDMS within the emulsion when starting the final curing process. We then attribute the presence of large pore size (Figure 1A−C) to the easier expansion of the water steam in a less reticulated PDMS. We believe that this factor may induce the aggregation of submillimetric water bubbles and the consequent formation of larger cavities.

By comparing the first column (A, D, G) and second column (B, E, H) of Figure 2, we investigate the impact of the different temperatures T_2 (110 and 130 °C) employed in the second reticulation process. By fixing t_1 = 30 min, we cannot find striking differences in pore size in Figure 2A,B, while this difference becomes more evident for higher prereticulation periods, as reported in Figure 2D−F. In Figure 2G, we can observe strong anisotropy, with elongated pores whose main semiaxis is 2- to 3-fold larger than the minor semiaxis. The pores of Figure 2F show lower anisotropy compared to Figure 2G but still much higher than the one of the pores in Figure 2B,E. We suggest that the temperature of final reticulation (T_2) has a double impact on the reaction: on the one hand, it slightly modifies the speed of evaporation of the water bubbles; on the other hand, it varies the kinetics of the reticulation of the silicone. As we observe from the comparison of Figure 2G,H, a lower temperature indeed tends to benefit the appearance of intrinsic anisotropy of the sample, which can be linked to a higher state of reticulation during the expansion of the water steam bubbles.

The third column (Figure 2C,F,I) explores the same temperature T_2 (130 °C) as in the second column (Figure 2B,E,H) but with a different pressure P_2 (700 mbar instead of 400 mbar). By observing the samples obtained with a short prereticulation time t_1 (Figure 2B,C), it is possible to highlight the impact of the pressure over the pore size. While the sample 2B features an average pore size of 1−3 mm, sample 2C presents a critical decrease of the typical size to 0.7−1.2 mm. For t_1 = 45 min, we observe the same tendency of reduced typical pore size within the PDMS porous scaffold, although this transition is less evident for the samples at 700 mbar (Figure 2C,F) than for the samples at 400 mbar (Figure 2B,E). Concerning the last row (Figure 2H,I), at long prereticulation time (60 min), we perceive a major reduction on the pore size coupled to a slight decrease in anisotropy of the pores. This behavior fits with the results obtained in the rest of the samples for those parameters.

The general overview of Figure 2 shows then a progressive decrement of the pore size by increasing the time of prereticulation t_1, which leads, at the same time, to an increase of the number of pores. We observe also an anisotropy tendency linked to the reticulation time (i.e., longer t_1 increases the reticulation state of the silicone before the evaporation of the steam). This induces less motility in the emulsion that in turn leads to a further expansion of the bubbles in the direction of the apertures of the PDMS sample holder. Temperature T_2, on the other hand, plays a dual role in the kinetics of the water evaporation and the kinetics of the reticulation process within the emulsion. Finally, pressure P_2 hinders the expansion of the bubbles, limiting the final pore size. From a microscopic point of view, the PDMS porous scaffold presents a hierarchical porous structuration. A close-up view of the bulk material between the larger pores for different fabrication parameters (t_1, T_2, P_2) reveals a network of interconnected pores featuring smaller dimensions (5−30 μm) with openings of 1−5 μm (see Figure S2). This induces a roughness on the surface that might influence the perfusion and diffusion of culture medium with a global impact for the cell environment.

To provide a more quantitative analysis of the pore size and spatial distribution, we performed a characterization of the

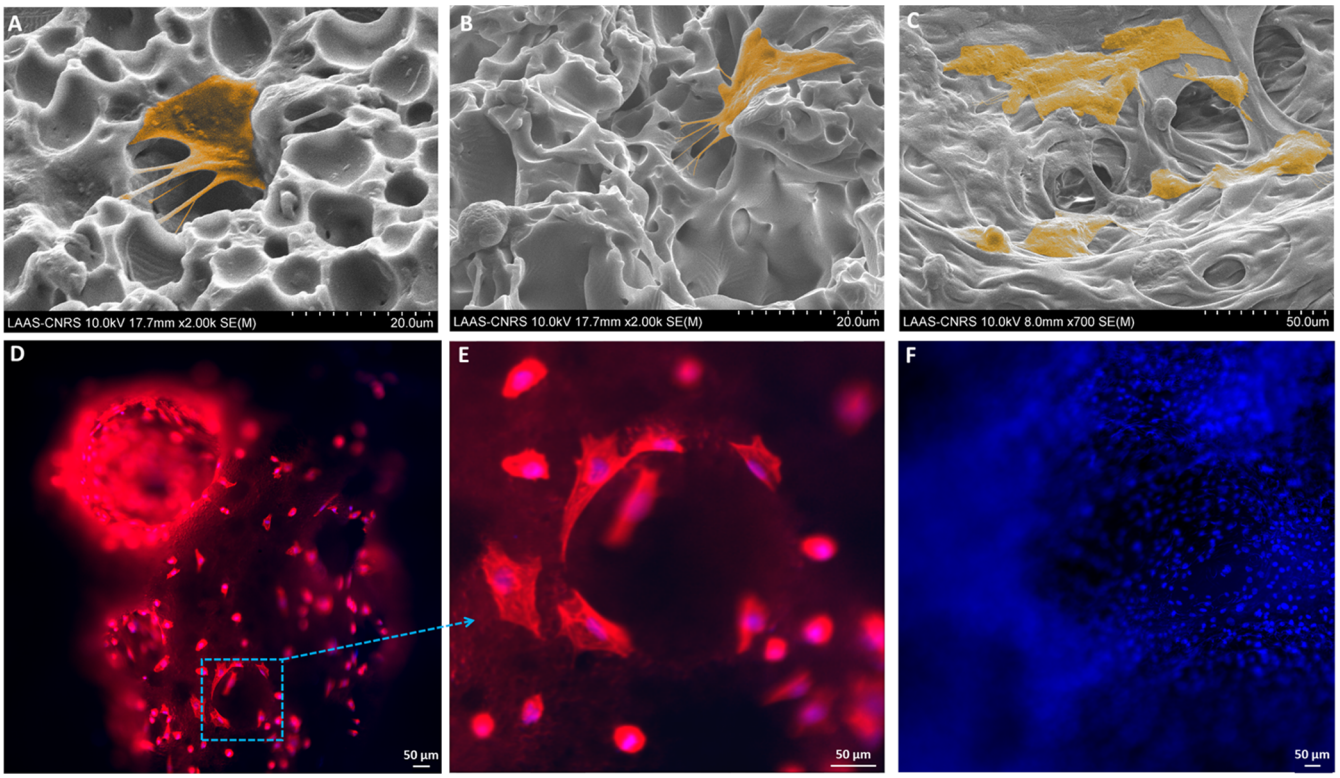

Figure 4. (A–C) False-colored SEM images highlighting the SaOS-2 cell morphology obtained on the PDMS porous scaffold; (D) immunofluorescence imaging of SaOS-2 cells colonizing the pores of the porous PDMS scaffold; (E) close-up view on the region enclosed in the blue dotted square in (D); (F) SaOS-2 "cellular-carpet" observed on the PDMS porous scaffold surface (red: phalloidin-F-actin; blue: DAPI-nuclei).

PDMS porous scaffold by employing X-ray tomography. The selected sample corresponds to the one of Figure 2B with t_1 = 30 min, T_2 = 130, and P_2 = 400 mbar, which was then employed as 3D cell culture support.

Figure S3A shows a reconstructed slice of the sample, after denoizing with a nonlocal means filter. A user-defined threshold was applied on each slice of the sample, leading to a stack of binarized images, as presented Figure S3B, corresponding to the slice shown in Figure S3A. The 3D reconstructed view of the PDMS porous scaffold in Figure 3A shows the porosity of the 3D architecture (whose optical micrograph is reported in Figure 3C). The crosscut views for the *xy* and *xz* planes show the inner core of the 3D architecture, proving a highly interconnected network with a wide spectrum of porosity. From those data, a porosity equal to around 57% was calculated from the binarized images (Figure S3C). A second validation of porosity using a watershed segmentation algorithm (for details, see Materials and Methods) was performed, resulting in a porosity equal to 58.7%, as presented in Figure 3D. Connectivity of pores was also studied with the Axis Connectivity module available in Avizo. Figure 3B shows in red the nonconnected pores and in white the connected ones. The total volume of pores is equal to 406.2 mm^3 in the sample, and nonconnected pores represent only 4.3 mm^3, corresponding to 1% of the total volume of pores. Nonconnected pores are either small pores <100 μm in the matrix or pores that are localized in the walls of the cylindrical support.

Finally, pore size distribution was analyzed. The histogram plot in Figure 3E represents the distribution of pore equivalent diameter, whose colorimetric 3D visualization linking pore diameters to different colors is reported in Figure 3D. The majority of the pores were reported to have a diameter between 0.02 and 0.10 mm (more detailed histograms are reported in Figure S4), although smaller pores (observed by SEM, Figure S2) could not be resolved due to resolution limitation (18 μm) of the X-ray microcomputed tomography setup (see Materials and Methods). These results were complemented with measurements of water retention performed over 48 h in the porous PDMS scaffold. As shown in Figure S5 and in the Supporting Video "Video_-liquid_loading", the percent of water remaining in the scaffold after soaking it in PBS for different periods of time increases until reaching a value close to ~300% (w:w). This value agrees with the high porosity and interconnectivity estimated by μCT.

3.2. SEM and Immunofluorescence Characterization of SaOS-2 Cell Colonization of the PDMS Scaffolds. To validate the compatibility of the developed PDMS architectures as a 3D cell culture tool, we tested the scaffold topology depicted in Figure 2B in the presence of SaOS-2 cells. Due to the morphology of the SaOS-2 cells and the topographical features of the PDMS porous scaffold, distinguishing the cells directly over a rugose surface is a laborious task. This is evident after comparing the morphologies of the osteosarcoma SaOS-2 cell line on untreated PDMS flat surfaces (Figure S6A) and on plasma treated/fibronectin-coated PDMS surfaces (Figure S6B). While on untreated surfaces we observe the same ratio of cells holding the expected flattened morphology and the less conventional globular one, on the treated surfaces we report only the flattened cytoskeletal configuration coupled to a more marked expression of typical round protrusions already observed elsewhere.[55] In such context, the role of roughness

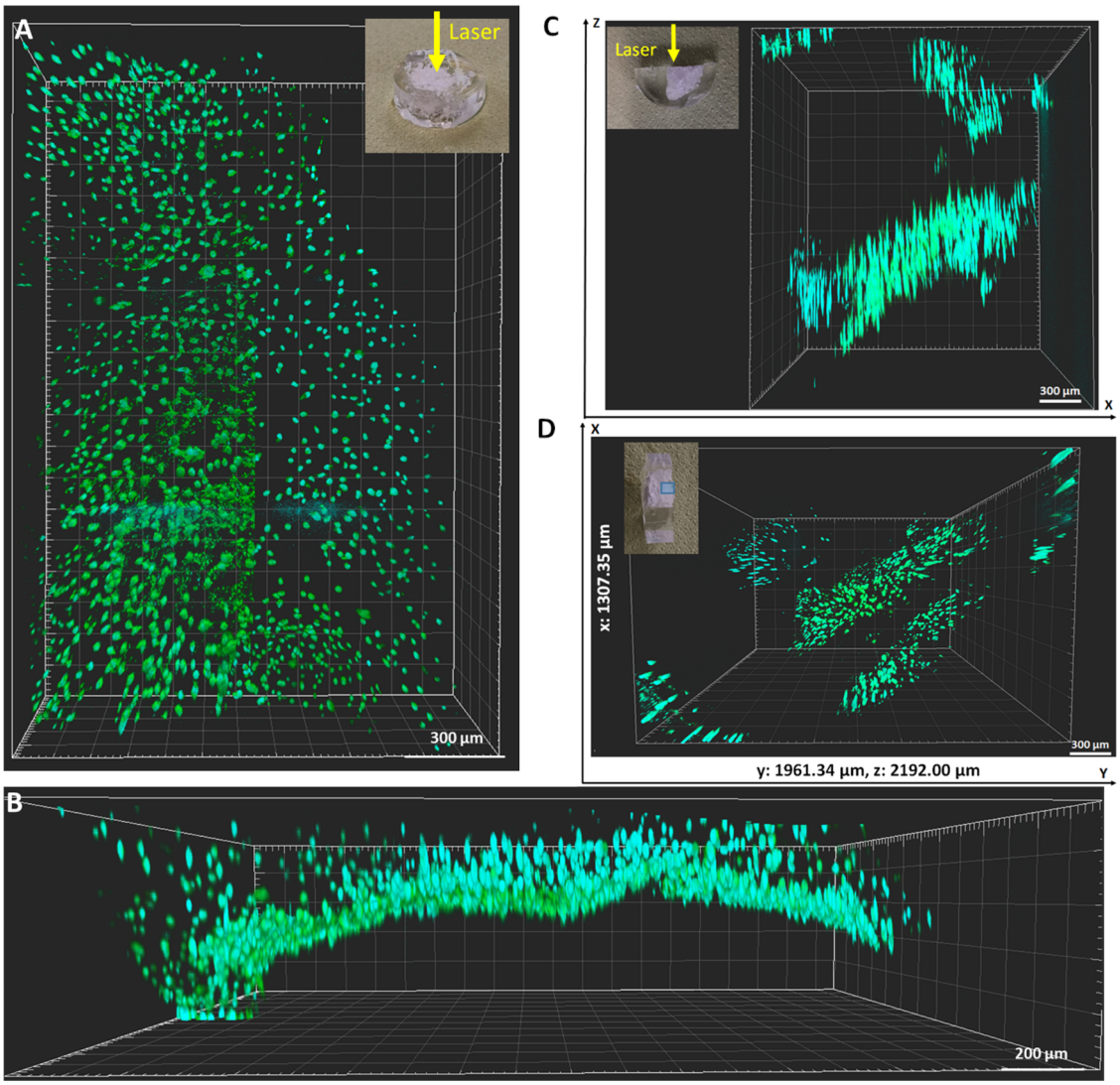

Figure 5. Two-photon confocal imaging of the PDMS porous scaffold colonized by SaOS-2 cells. (A) *xy* view of the 3D reconstruction of the scaffold imaged with the laser beam impinging the sample as shown in the inset; (B) *xz* view of the 3D reconstruction in (A); (C) *xz* view of the 3D reconstruction of a cross-cut of the scaffold imaged with the laser beam impinging the sample as shown in the inset; (D) *xy* view of the 3D reconstruction in (C) (the inset shows the sample orientation and the region depicted in the 3D reconstruction (green: CMFDA; blue: DAPI-nuclei)).

and surface chemistry regulating cell adhesion mechanisms has been previously observed for nonpolymeric surfaces.[56,57]

In addition to its role in the adsorption of adhesion proteins, plasma treatments are indeed known to induce the presence of nanotopography features and surface chemistry changes, which are reflected in an augmentation of oxygen content and an enhancement of surface energy associated with an increase in wettability that influences cell adhesion on polymeric surfaces.[58,59] Concerning the distribution and welfare of cells within the PDMS porous scaffold, in Figure 4A–C, we present false-colored SEM close-up images highlighting the typical cell morphology that we observed in different regions of the scaffold. SaOS-2 cells tend to develop cytoskeletal extensions anchoring to the side walls of the micropores in a tridimensional spatial configuration, as observed in Figure 4A,B. The evidence of the flattened elongated morphology of a cluster of cells in other regions of the scaffold characterized by PDMS meshes is shown in Figure 4C. Furthermore, we can discriminate several round protuberances within the cellular cytoskeleton that we associate with regular features of mineralized buds and calcospherulites related to the process of mineral deposition of this cell line.[60,61] This behavior could be associated with a predifferentiation stage, although a deeper evaluation of differentiation markers is required to confirm this assessment. Prospective analysis of the calcification process by red alizarin staining will be carried out in the future to validate this conclusion. Furthermore, cell viability test, shown in Figure S7, was addresses by Live/Dead assay on the porous PDMS scaffold against two positive controls, flat PDMS and glass. Cell viability reached ∼99% of the cell population over the porous PDMS scaffold. This result compares with the performance of both positive controls showing as well a cell viability of ∼99% and a more homogeneous cell distribution.

To better visualize typical morphological features of the SaOS cells cultured on the 3D scaffold, in Figure 4D–F, we report the epifluorescence characterization of the osteosarcoma cells over the PDMS porous scaffold. In Figure 4D, we can observe the cell spreading and colonization of different pores,

where the F-actin, the main component of microfilaments in the cytoskeleton, is stained in red with phalloidin/rhodamine while the nuclei are stained in blue with DAPI. We can distinguish several cells colonizing the full structure at different out-focus planes. In Figure 4E, we show the close-up view of a single pore (enclosed by the blue square in Figure 4D) depicting how the elongated cytoskeleton of the cells adapts to the surrounding environments by following the geometrical profile of the pore. Finally, in Figure 4F, we present a fluorescence image of another region of the scaffold where we can easily identify cell nuclei and observe how cells cover homogeneously the whole surface of the PDMS porous scaffold.

To get a clear view of the 3D cell colonization scenario of the PDMS porous scaffold, in Figure 5, we report several 3D reconstructions obtained via two-photon confocal imaging, a widely used technique for unveiling cell features in the inner core of 3D architectures otherwise not accessible by more conventional morphological imaging approaches (e.g., SEM and AFM).[33,35] In Figure 5A,B, we report the characterization of the upper part of the 3D scaffold (i.e., the one on which the cell medium containing the SaOS-2 cells was deposited), impinged by the laser beam as shown in the inset of Figure 5A, where we highlighted the nuclear marker DAPI (in blue) and the CMFDA one (in green), which is able to stain the whole cytoplasm of the cells (Figure S8). The overall field of view of the acquisition is 1.96 × 1.30 × 0.49 mm^3 (obtained by employing a mosaic modality where we imaged smaller areas and then stitched them together). Figure 5A shows a quite homogeneous cell coverage of the PDMS scaffold surface, while Figure 5B highlights how cells are able to colonize the inner part of the architecture by infiltrating open pores (such as the one on the left-hand side of the figure). We attribute the absence of cells in the central part of the 3D reconstruction either to the small dimensions of the pores (compared to the SaOS-2 cell size) in that region or, more likely, to the fact that denser regions of PDMS (becoming opaque during the fabrication because of the trapping of air bubbles) hinder the passage of photons. A clearer overview of the 3D imaging acquisition can be seen in the Supporting Video "Video_top_surface". To have a further insight into the cellular distribution within the 3D scaffold, we performed also a cross-cut on it by using a surgical blade to reveal the inner part of the structure. Figure 5C,D shows, respectively, the *x*, *z* and *x*, *y* views of a 1.30 × 1.96 × 2.19 mm^3 region of the PDMS porous scaffold (always by employing the mosaic modality mentioned above) with the laser impinging this time the inner surface of the cross-cut, as depicted in the inset of Figure 5C. The two different views show the presence of omnidirectional cell clusters infiltrating both the superficial layers of the scaffold and the inner areas down to a depth ≈2.2 mm along the *z* axis and ≈2 mm along the *y* axis. A high-resolution video ("Video_cross_cut") of the slices composing the 3D reconstruction is available in the Supporting Information.

4. CONCLUSIONS

In this work, we reported a novel 3D structuration technique that provides a fast and cheap process to fabricate porous scaffolds made of a widely used biocompatible silicone such as PDMS. This technique involves a simple combination of water and silicone to form an emulsion that is further transformed into a highly porous scaffold using a two-step reticulation process. The fabrication takes place under temperature-/pressure-controlled environment that could be easily scalable for mass production. Scanning electron microscopy characterization provided a deep understanding of the different achieved morphologies confirming a control of the porous distribution associated with a hierarchical macro-micro structuration of the available surface that could have an impact on the biological perfusion and diffusion of nourishment. 3D morphological characterization was carried out by X-ray computed tomography and allowed to evaluate the general porosity and the size distribution of the pores as well as to investigate the interconnectivity of the PDMS porous scaffold. The format chosen to evaluate the performance of cell culture presented a general porosity of ∼60% with a ∼98% global interconnectivity. Osteosarcoma SaOS-2 cells were seeded on the PDMS porous scaffold to evaluate the efficiency of the cell colonization and perfusion. SEM investigation in combination with fluorescence immune-staining imaging demonstrated a high level of cell adhesion and some features of advanced cell maturation. Two-photon confocal reconstruction displayed information about the cell colonization taking place within volumes of several mm^3 in the inner core of the scaffold, proving a homogeneous tridimensional distribution of cells and their proliferation through all of the available pores.

As the fabrication process is simple, adapted with injection techniques, and amenable to large-scale production, we believe that it will open intriguing opportunities aiming at the integration of 3D porous scaffolds in bioreactors or micro-physiological systems. Further studies will be devoted to the impact of the scaffold porosity and architecture on inner flow patterns provided by microfluidic systems and subsequent studies on cell proliferation and differentiation.

Supporting Information

3D model of the 3D-printed mold employed for the fabrication of the PDMS sample holder; SEM close-up images of the PDMS nest scaffold for different reticulation conditions; X-ray tomography analysis, porosity, and pore diameter distribution; and SEM and immunofluorescence characterization of SaOS-2 cells (PDF)

Video_top_surface (MP4)

Video_cross_cut (MP4)

Video_liquid_loading (MP4)

AUTHOR INFORMATION

Corresponding Authors

*E-mail: A.Accardo@tudelft.nl. Phone: +31(0)152781610 (A.A.).

*E-mail: laurent.malaquin@laas.fr, lmalaquin@laas.fr. Phone: +33(0)561336384. Fax: +33(0)561553577 (L.M.).

ORCID

Thierry Leichle: 0000-0003-3183-8976

Angelo Accardo: 0000-0003-0442-3652

Present Address

[⊥]Department of Precision and Microsystems Engineering, Delft University of Technology, Mekelweg 2, 2628 CD Delft, The Netherlands (A.A.).

Author Contributions

The manuscript was written through contributions of all authors. All authors have given approval to the final version of the manuscript.

Funding

The present work was supported by the H2020 European project HOLIFab (Grant No. 760927). It was as well partly supported as part of the MultiFAB project funded by FEDER European Regional Funds and French Région Occitanie (grant agreement number: 16007407/MP0011594).

Notes

The authors declare no competing financial interest.

■ ACKNOWLEDGMENTS

This work was partly supported by the LAAS-CNRS micro- and nanotechnologies platform member of the French RENATECH network. The authors acknowledge the support of Sophie Allart and Daniele Daviaud from the INSERM Centre de Physiopathologie de Toulouse-Purpan (CPTP) of Toulouse during the multiphoton confocal imaging acquisitions. They also acknowledge the support of FERMAT Federation to this work.

■ REFERENCES

(1) Xiang, Z.; Cao, D. Porous Covalent−Organic Materials: Synthesis, Clean Energy Application and Design. *J. Mater. Chem. A* **2013**, *1*, 2691−2718.

(2) Wang, W.; Zhou, M.; Yuan, D. Carbon Dioxide Capture in Amorphous Porous Organic Polymers. *J. Mater. Chem. A* **2017**, *5*, 1334−1347.

(3) Kim, S.; Lee, Y. M. Rigid and Microporous Polymers for Gas Separation Membranes. *Prog. Polym. Sci.* **2015**, *43*, 1−32.

(4) Kaur, P.; Hupp, J. T.; Nguyen, S. T. Porous Organic Polymers in Catalysis: Opportunities and Challenges. *ACS Catal.* **2011**, *1*, 819−835.

(5) Lande, B.; Mitzner, W. Analysis of Lung Parenchyma as a Parametric Porous Medium. *J. Appl. Physiol.* **2006**, *101*, 926−933.

(6) Zhao, M.; Li, L. Dissecting the Bone Marrow HSC Niches. *Cell Res.* **2016**, *26*, 975−976.

(7) Loh, Q. L.; Choong, C. Three-Dimensional Scaffolds for Tissue Engineering Applications: Role of Porosity and Pore Size. *Tissue Eng., Part B* **2013**, *19*, 485−502.

(8) Zhu, D.; Handschuh-Wang, S.; Zhou, X. Recent Progress in Fabrication and Application of Polydimethylsiloxane Sponges. *J. Mater. Chem. A* **2017**, *5*, 16467−16497.

(9) McDonald, J. C.; Anderson, D. C. D. J. R.; Chiu, D. T.; Wu, H.; Schueller, O. J. A.; Whitesides, G. M. Fabrication of Microfluidic Systems in Poly(Dimethylsiloxane). *Electrophoresis* **2000**, *21*, 27−40.

(10) Jung, S.; Kim, J. H.; Kim, J.; Choi, S.; Lee, J.; Park, I.; Hyeon, T.; Kim, D.-H. Reverse-Micelle-Induced Porous Pressure-Sensitive Rubber for Wearable Human-Machine Interfaces. *Adv. Mater.* **2014**, *26*, 4825−4830.

(11) Shi, J.; Zhang, H.; Jackson, J.; Shademani, A.; Chiao, M. A Robust and Refillable Magnetic Sponge Capsule for Remotely Triggered Drug Release. *J. Mater. Chem. B* **2016**, *4*, 7415−7422.

(12) Liu, W.; Chen, Z.; Zhou, G.; Sun, Y.; Lee, H. R.; Liu, C.; Yao, H.; Bao, Z.; Cui, Y. 3D Porous Sponge-Inspired Electrode for Stretchable Lithium-Ion Batteries. *Adv. Mater.* **2016**, *28*, 3578−3583.

(13) Liang, S.; Li, Y.; Chen, Y.; Yang, J.; Zhu, T.; Zhu, D.; He, C.; Liu, Y.; Handschuh-Wang, S.; Zhou, X. Liquid Metal Sponges for Mechanically Durable, All-Soft, Electrical Conductors. *J. Mater. Chem. C* **2017**, *5*, 1586−1590.

(14) Duan, S.; Yang, K.; Wang, Z.; Chen, M.; Zhang, L.; Zhang, H.; Li, C. Fabrication of Highly Stretchable Conductors Based on 3D Printed Porous Poly(Dimethylsiloxane) and Conductive Carbon Nanotubes/Graphene Network. *ACS Appl. Mater. Interfaces* **2016**, *8*, 2187−2192.

(15) Han, J.-W.; Kim, B.; Li, J.; Meyyappan, M. Flexible, Compressible, Hydrophobic, Floatable, and Conductive Carbon Nanotube-Polymer Sponge. *Appl. Phys. Lett.* **2013**, *102*, No. 051903.

(16) McCall, W. R.; Kim, K.; Heath, C.; La Pierre, G.; Sirbuly, D. J. Piezoelectric Nanoparticle−Polymer Composite Foams. *ACS Appl. Mater. Interfaces* **2014**, *6*, 19504−19509.

(17) Bélanger, M. C.; Marois, Y. Hemocompatibility, Biocompatibility, Inflammatory and in Vivo Studies of Primary Reference Materials Low-Density Polyethylene and Polydimethylsiloxane: A Review. *J. Biomed. Mater. Res.* **2001**, *58*, 467−477.

(18) Mata, A.; Fleischman, A. J.; Roy, S. Characterization of Polydimethylsiloxane (PDMS) Properties for Biomedical Micro/Nanosystems. *Biomed. Microdevices* **2005**, *7*, 281−293.

(19) Vaysse, L.; Beduer, A.; Sol, J. C.; Vieu, C.; Loubinoux, I. Micropatterned Bioimplant with Guided Neuronal Cells to Promote Tissue Reconstruction and Improve Functional Recovery after Primary Motor Cortex Insult. *Biomaterials* **2015**, *58*, 46−53.

(20) Zhou, J.; Ellis, A. V.; Voelcker, N. H. Recent Developments in PDMS Surface Modification for Microfluidic Devices. *Electrophoresis* **2010**, *31*, 2−16.

(21) Halldorsson, S.; Lucumi, E.; Gómez-Sjöberg, R.; Fleming, R. M. T. Advantages and Challenges of Microfluidic Cell Culture in Polydimethylsiloxane Devices. *Biosens. Bioelectron.* **2015**, *63*, 218−231.

(22) Lötters, J. C.; Olthuis, W.; Veltink, P. H.; Bergveld, P. The Mechanical Properties of the Rubber Elastic Polymer Polydimethylsiloxane for Sensor Applications. *J. Micromech. Microeng.* **1997**, *7*, 145−147.

(23) Merkel, T. C.; Bondar, V. I.; Nagai, K.; Freeman, B. D.; Pinnau, I. Gas Sorption, Diffusion, and Permeation in Poly(Dimethylsiloxane) The Permeability of Poly(Dimethylsiloxane) [PDMS] To. *J. Polym. Sci., Part B: Polym. Phys.* **2000**, *38*, 415−434.

(24) Piruska, A.; Nikcevic, I.; Lee, S. H.; Ahn, C.; Heineman, W. R.; Limbach, P. A.; Seliskar, C. J. The Autofluorescence of Plastic Materials and Chips Measured under Laser Irradiation. *Lab Chip* **2005**, *5*, 1348.

(25) Haycock, J. W. 3D Cell Culture: A Review of Current Approaches and Techniques. In *3D Cell Culture*; Humana Press, 2010; pp 1−15.

(26) McKee, C.; Chaudhry, G. R. Advances and Challenges in Stem Cell Culture. *Colloids Surf., B* **2017**, *159*, 62−77.

(27) Ingber, D. E. Cellular Mechanotransduction: Putting All the Pieces Together Again. *FASEB J.* **2006**, *20*, 811−827.

(28) Ranga, A.; Gobaa, S.; Okawa, Y.; Mosiewicz, K.; Negro, A.; Lutolf, M. P. 3D Niche Microarrays for Systems-Level Analyses of Cell Fate. *Nat. Commun.* **2014**, *5*, No. 4324.

(29) Do, A.-V.; Khorsand, B.; Geary, S. M.; Salem, A. K. 3D Printing of Scaffolds for Tissue Regeneration Applications. *Adv. Healthcare Mater.* **2015**, *4*, 1742−1762.

(30) Wang, Z.; Abdulla, R.; Parker, B.; Samanipour, R.; Ghosh, S.; Kim, K. A Simple and High-Resolution Stereolithography-Based 3D Bioprinting System Using Visible Light Crosslinkable Bioinks. *Biofabrication* **2015**, *7*, No. 045009.

(31) Accardo, A.; Courson, R.; Riesco, R.; Raimbault, V.; Malaquin, L. Direct Laser Fabrication of Meso-Scale 2D and 3D Architectures with Micrometric Feature Resolution. *Addit. Manuf.* **2018**, *22*, 440−446.

(32) Lemma, E. D.; Spagnolo, B.; De Vittorio, M.; Pisanello, F. Studying Cell Mechanobiology in 3D: The Two-Photon Lithography Approach. *Trends Biotechnol.* **2019**, *37*, 358−372.

(33) Accardo, A.; Blatché, M. C.; Courson, R.; Loubinoux, I.; Vieu, C.; Malaquin, L. Two-Photon Lithography and Microscopy of 3D Hydrogel Scaffolds for Neuronal Cell Growth. *Biomed. Phys. Eng. Express* **2018**, *4*, No. 027009.

(34) Accardo, A.; Blatché, M.-C.; Courson, R.; Loubinoux, I.; Vieu, C.; Malaquin, L. Direct Laser Fabrication of Free-Standing PEGDA-

Hydrogel Scaffolds for Neuronal Cell Growth: Engineering 3D Biocompatible Microenvironments. *Mater. Today* **2018**, *21*, 315−316.
(35) Accardo, A.; Blatché, M.-C.; Courson, R.; Loubinoux, I.; Thibault, C.; Malaquin, L.; Vieu, C. Multiphoton Direct Laser Writing and 3D Imaging of Polymeric Freestanding Architectures for Cell Colonization. *Small* **2017**, *13*, No. 1700621.
(36) Jia, W.; Gungor-Ozkerim, P. S.; Zhang, Y. S.; Yue, K.; Zhu, K.; Liu, W.; Pi, Q.; Byambaa, B.; Dokmeci, M. R.; Shin, S. R.; et al. Direct 3D Bioprinting of Perfusable Vascular Constructs Using a Blend Bioink. *Biomaterials* **2016**, *106*, 58−68.
(37) Carve, M.; Wlodkowic, D. 3D-Printed Chips: Compatibility of Additive Manufacturing Photopolymeric Substrata with Biological Applications. *Micromachines* **2018**, *9*, 91.
(38) Tebboth, M.; Jiang, Q.; Kogelbauer, A.; Bismarck, A. Inflatable Elastomeric Macroporous Polymers Synthesized from Medium Internal Phase Emulsion Templates. *ACS Appl. Mater. Interfaces* **2015**, *7*, 19243−19250.
(39) Zargar, R.; Nourmohammadi, J.; Amoabediny, G. Preparation, Characterization, and Silanization of 3D Microporous PDMS Structure with Properly Sized Pores for Endothelial Cell Culture. *Biotechnol. Appl. Biochem.* **2016**, *63*, 190−199.
(40) Mohanty, S.; Larsen, L. B.; Trifol, J.; Szabo, P.; Burri, H. V. R.; Canali, C.; Dufva, M.; Emnéus, J.; Wolff, A. Fabrication of Scalable and Structured Tissue Engineering Scaffolds Using Water Dissolvable Sacrificial 3D Printed Moulds. *Mater. Sci. Eng., C* **2015**, *55*, 569−578.
(41) Dahlberg, T.; Stangner, T.; Zhang, H.; Wiklund, K.; Lundberg, P.; Edman, L.; Andersson, M. 3D Printed Water-Soluble Scaffolds for Rapid Production of PDMS Micro-Fluidic Flow Chambers. *Sci. Rep.* **2018**, *8*, No. 3372.
(42) Díaz Lantada, A.; Alarcón Iniesta, H.; Pareja Sánchez, B.; García-Ruíz, J. P. Free-Form Rapid Prototyped Porous PDMS Scaffolds Incorporating Growth Factors Promote Chondrogenesis. *Adv. Mater. Sci. Eng.* **2014**, *2014*, 1−10.
(43) Li, Q.; Duan, T.; Shao, J.; Yu, H. Fabrication Method for Structured Porous Polydimethylsiloxane (PDMS). *J. Mater. Sci.* **2018**, *53*, 11873−11882.
(44) Chen, I.-J.; Lindner, E. The Stability of Radio-Frequency Plasma-Treated Polydimethylsiloxane Surfaces. *Langmuir* **2007**, *23*, 3118−3122.
(45) Kim, D. H.; Jung, M. C.; Cho, S.-H.; Kim, S. H.; Kim, H.-Y.; Lee, H. J.; Oh, K. H.; Moon, M.-W. UV-Responsive Nano-Sponge for Oil Absorption and Desorption. *Sci. Rep.* **2015**, *5*, No. 12908.
(46) Pedraza, E.; Brady, A.-C.; Fraker, C. A.; Stabler, C. L. Synthesis of Macroporous Poly(Dimethylsiloxane) Scaffolds for Tissue Engineering Applications. *J. Biomater. Sci., Polym. Ed.* **2013**, *24*, 1041−1056.
(47) Pedraza, E.; Brady, A.-C.; Fraker, C. A.; Molano, R. D.; Sukert, S.; Berman, D. M.; Kenyon, N. S.; Pileggi, A.; Ricordi, C.; Stabler, C. L. Macroporous Three-Dimensional PDMS Scaffolds for Extrahepatic Islet Transplantation. *Cell Transplant.* **2013**, *22*, 1123−1135.
(48) Carnachan, R. J.; Bokhari, M.; Przyborski, S. A.; Cameron, N. R. Tailoring the Morphology of Emulsion-Templated Porous Polymers. *Soft Matter* **2006**, *2*, 608.
(49) Silverstein, M. S. PolyHIPEs: Recent Advances in Emulsion-Templated Porous Polymers. *Prog. Polym. Sci.* **2014**, *39*, 199−234.
(50) Rodan, S. B.; Imai, Y.; Thiede, M. A.; Wesolowski, G.; Thompson, D.; Bar-Shavit, Z.; Shull, S.; Mann, K.; Rodan, G. A. Characterization of a Human Osteosarcoma Cell Line (Saos-2) with Osteoblastic Properties. *Cancer Res.* **1987**, *47*, 4961−4966.
(51) Prideaux, M.; Wijenayaka, A. R.; Kumarasinghe, D. D.; Ormsby, R. T.; Evdokiou, A.; Findlay, D. M.; Atkins, G. J. SaOS2 Osteosarcoma Cells as an in Vitro Model for Studying the Transition of Human Osteoblasts to Osteocytes. *Calcif. Tissue Int.* **2014**, *95*, 183−193.
(52) Buades, A.; Coll, B.; Morel, J. M. In *A Non-Local Algorithm for Image Denoising*, Proceedings - 2005 IEEE Computer Society Conference on Computer Vision and Pattern Recognition, CVPR 2005, 2005; Vol. *II*, pp 60−65.
(53) Schlüter, S.; Sheppard, A.; Brown, K.; Wildenschild, D. Image Processing of Multiphase Images Obtained via X-Ray Microtomography: A Review. *Water Resour. Res.* **2014**, 3615−3639.
(54) Varshney, N.; Sahi, A. K.; Vajanthri, K. Y.; Poddar, S.; Balavigneswaran, C. K.; Prabhakar, A.; Rao, V.; Mahto, S. K. Culturing Melanocytes and Fibroblasts within Three-Dimensional Macroporous PDMS Scaffolds: Towards Skin Dressing Material. *Cytotechnology* **2019**, *71*, 287−303.
(55) Wiggan, O.; Hamel, P. A. Pax3 Regulates Morphogenetic Cell Behavior in Vitro Coincident with Activation of a PCP/Non-Canonical Wnt-Signaling Cascade. *J. Cell Sci.* **2002**, *115*, 531−541.
(56) Onesto, V.; Cancedda, L.; Coluccio, M. L.; Nanni, M.; Pesce, M.; Malara, N.; Cesarelli, M.; Di Fabrizio, E.; Amato, F.; Gentile, F. Nano-Topography Enhances Communication in Neural Cells Networks. *Sci. Rep.* **2017**, *7*, No. 9841.
(57) Onesto, V.; Villani, M.; Narducci, R.; Malara, N.; Imbrogno, A.; Allione, M.; Costa, N.; Coppedè, N.; Zappettini, A.; Cannistraci, C. V.; et al. Cortical-like Mini-Columns of Neuronal Cells on Zinc Oxide Nanowire Surfaces. *Sci. Rep.* **2019**, *9*, No. 4021.
(58) Kim, J.-H.; Seo, S.; Min, J. Epithelial Cell Patterns on a PDMS Polymer Surface Using a Micro Plasma Structure. *J. Biotechnol.* **2011**, *155*, 308−311.
(59) Accardo, A.; Shalabaeva, V.; La Rocca, R. Colon Cancer Cells Adhesion on Polymeric Nanostructured Surfaces. *MRS Commun.* **2018**, *8*, 35−39.
(60) Schröder, H. C.; Boreiko, O.; Krasko, A.; Reiber, A.; Schwertner, H.; Müller, W. E. G. Mineralization of SaOS-2 Cells on Enzymatically (Silicatein) Modified Bioactive Osteoblast-Stimulating Surfaces. *J. Biomed. Mater. Res., Part B* **2005**, *75*, 387−392.
(61) Barreau, C.; Labit, E.; Guissard, C.; Rouquette, J.; Boizeau, M. L.; Gani Koumassi, S.; Carrière, A.; Jeanson, Y.; Berger-Müller, S.; Dromard, C.; et al. Regionalization of Browning Revealed by Whole Subcutaneous Adipose Tissue Imaging. *Obesity* **2016**, *24*, 1081−1089.